The catalytic effects of active site conformational change in the allosteric activation of imidazole glycerol phosphate synthase

Heidi Klem,*[,1] Juan V. Alegre-Requena,*[,2] Robert S. Paton*[,1]

[1]Department of Chemistry, Colorado State University, Fort Collins, CO 80523, USA.

[2]Dpto.de Química Inorgánica, Instituto de Síntesis Química y Catálisis Homogénea (ISQCH), CSIC, Universidad de Zaragoza, Zaragoza, 50009, Spain

ABSTRACT: Imidazole glycerol phosphate synthase (IGPS) is a heterodimeric class-I glutamine amidotransferase (GAT) that hydrolyzes glutamine. Ammonia is produced and transferred to a second active site where it reacts with N[1]-(5'-phosphoribosyl)-formimino-5-aminoimidazole-4 carboxamide ribonucleotide (PrFAR) to form precursors to purine and histidine biosynthesis. Binding of PrFAR over 25 Å away from the active site increases glutaminase efficiency by ~4500-fold, primarily altering the glutamine turnover number. IGPS has been the focus of many studies on allosteric communication; however, atomic details for how the glutamine hydrolysis rate increases in the presence of PrFAR are lacking. We present a density functional theory study on 237-atom active site cluster models of IGPS based on crystallized structures representing the inactive and allosterically-active conformations and investigate the multistep reaction leading to thioester formation and ammonia production. The proposed mechanism is supported by similar, well-studied enzyme mechanisms, and the corresponding energy profile is consistent with steady-state kinetic studies of PrFAR+IGPS. Additional active site models are constructed to examine the relationship between active site structural change and transition state stabilization via energy decomposition schemes. The results reveal that the inactive IGPS conformation does not provide an adequately formed oxyanion hole structure and that repositioning of the oxyanion strand relative to the substrate is vital for a catalysis-competent oxyanion hole, with or without the hVal51 dihedral flip. These findings are valuable for future endeavors in modeling the IGPS allosteric mechanism by providing insight into the atomistic changes required for rate enhancement that can inform suitable reaction coordinates for subsequent investigations.

KEYWORDS: *allostery · conformational change · theozyme · quantum chemical cluster approach · oxyanion hole*

INTRODUCTION

Imidazole glycerol phosphate synthase (IGPS) is a glutamine amidotransferase (GAT) vital to purine and histidine biosynthetic pathways in bacteria, fungi, and plants, making it an attractive antimicrobial therapeutic target.[1] IGPS from *Thermotoga maritima* is a heterodimer composed of the HisH and HisF subunits (HisFH) (Figure 1).[2] HisH performs glutamine (*L*-Gln) hydrolysis to form glutamate (*L*-Glu) and ammonia using a catalytic triad of *h*Cys84, *h*His178, and *h*Glu180 (*h* and *f* prefixes indicate if the residue belongs to HisH or HisF, respectively), characterizing it as a class-I GAT.[3,4] The free ammonia is shuttled across the dimer interface to react with N[1]-(5'-phosphoribosyl)-formimino-5-aminoimidazole-4 carboxamide ribonucleotide (PrFAR) in the HisF active site over 25 Å away to form imidazole glycerol phosphate (IGP) and 5'-(5-aminoimidazole-4-carboxamide) ribonucleotide (AICAR).[5] Binding of PrFAR to HisF elicits a V-type allosteric effect that enhances glutamine hydrolysis efficiency in HisH by approximately 4500-fold, primarily influencing the rate of glutamine turnover.[2,6]

The hydrolysis reaction mechanism has not yet been studied at the atomic level in IGPS, to the best of our knowledge. However, similar well-studied enzymes, such as other class-I GATs and cysteine/serine proteases provide a useful theoretical foundation.[3,4,7–13] These reactions are proposed to

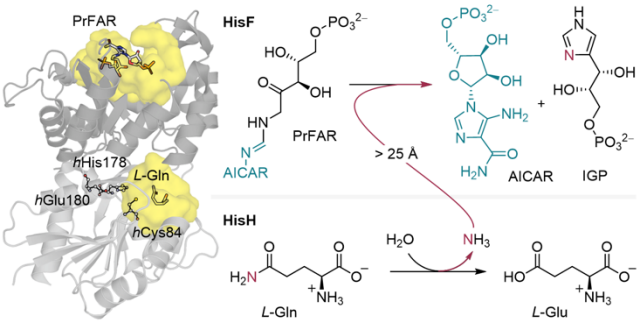

Figure 1. General IGPS scheme of the coupled *L*-Gln hydrolysis and PrFAR cyclization reactions performed in HisH. and HisF, respectively. The *L*-Gln and PrFAR binding sites are highlighted in yellow.

occur via two stages: acylation and deacylation. In the acylation stage, the nucleophilic *h*Cys84 attacks glutamine to form a glutamyl thioester, first structurally observed in another class-I GAT, carbamoyl phosphate synthetase,[10] via a tetrahedral oxyanion intermediate. In the deacylation stage, nucleophilic attack by a water molecule breaks down the covalent enzyme-substrate intermediate thioester, to yield the glutamate product. The rate-limiting step is proposed to occur during acylation in IGPS,[14] as well as related class-I

GATs, carbamyl phosphate synthetase, and anthranilate synthase.[3,11,15]

IGPS serves as a paradigmatic allosteric enzyme for experimental and methodological developments.[16–27] An abundance of dynamical information contribute to our understanding of the allosteric mechanism in IGPS at the molecular level. A sequence of residues (*h*Pro49—*h*Gly50—*h*Val51—*h*Gly52 in IGPS) comprise the oxyanion strand, a structural motif common to class-I GATs that positions a backbone amide hydrogen to stabilize the formation of an oxyanion throughout the reaction.[28–32] Increased flexibility in the IGPS oxyanion strand upon PrFAR binding was observed in NMR experiments and molecular dynamics (MD) simulations, supporting its mechanistic involvement.[25,33,34] An interfacial hydrogen bond between *f*Pro10 and the backbone N–H of *h*Val51 is weakened in MD simulations with PrFAR,[26,35] and explains the enhanced flexibility of the oxyanion strand observed in NMR experiments.[25,34] PrFAR also reduces the opening angle of the interface, which is expected to influence the hydrolysis reaction, although it is unclear if there is a direct effect on the reaction mechanism.[6,19,33,36]

A leading hypothesis to explain the allosteric rate effect in IGPS is that PrFAR enables a conformational change in the *h*Val51 backbone that lowers the rate of glutamine hydrolysis via a catalytically competent oxyanion hole.[14,35,37,38] Contrary to this hypothesis, the *h*Val51 amide C=O group points into the active site and the N–H away in all but one crystallographic conformations of IGPS in various ligand bound states.[5,6,39–41] The anamolous conformation is observed in a recently deposited structure 7ac8, chains E and F with bound allosteric ligand and Gln substrate.[14] The catalytic *h*Cys84 was mutated to alanine in this structure to disable glutamine turnover and capture IGPS in the presumably active conformation. Osuna and coworkers provide additional support for this hypothesis through MD simulations employing a biasing potential to sample the *h*Val51 dihedral flip transition. The energetic barrier of this process was estimated to be lower in simulations with PrFAR present (approx. 8 kcal/mol) compared to without PrFAR present (approx. 22 kcal/mol).[35]

Exploration of an alternative activation mechanism is warranted for a few reasons. Extensive (10 μs) unbiased MD simulations of IGPS only reproduced the *h*Val51 dihedral transition when neither Gln nor PrFAR were present, contrary to what was expected.[24] The authors noted the novel IGPS conformation revealed in the 7ac8 crystallographic model could be an artifact of the loss of function *h*Cys84Ala mutation rather than intrinsic to the allosteric mechanism. An alternative activation mechanism that has yet to be evaluated in IGPS involves repositioning of the oxyanion strand relative to the Gln substrate. This activation hypothesis has been proposed for another class-I GAT, aminodeoxychorismate synthase (ADCS) since the presence of two prolines in its oxyanion strand (Pro51—Gly52—Pro53) inhibits Gly52 backbone rotation.[42] All Gln bound IGPS structures show a hydrogen bond between the *h*Gly52 N–H and Gln carbonyl; however, Gln is presumed to be too far from *h*Cys84 to facilitate the nucleophilic attack. The increased oxyanion strand flexibility observed in the presence of PrFAR could facilitate the oxyanion strand reorganization necessary to stabilize the substrate after nucleophilic attack.

Despite various X-ray structures, mutagenesis studies, kinetic experiments, and MD simulations, a connection between the allosteric effect and the glutamine hydrolysis mechanism remains hypothetical. This work targets two essential questions regarding IGPS activation*: How do local structural aspects of the active site influence the reaction energetics? Is the hVal51 backbone flip required for rate enhancement?* To address these questions, we present a dispersion-corrected Density Functional Theory (DFT) study on large (237 atoms) active site cluster models of IGPS in various active and inactive conformations. The multistep reaction leading to thioester formation and ammonia production is investigated and energy decomposition analyses are performed to evaluate the relationship between active site geometry and reaction stabilization. Our results are valuable for future endeavors in modeling the allosteric behavior of this prototypical system by providing clear insights into the atomistic changes required for rate enhancement.

Although rigorous workflows have been devised to consider active site multi-state effects on catalysis,[43–46] this work affords a simplified approach given the available crystallographic data and scope of knowledge from preceding investigations. In doing so, our application of the quantum chemical cluster approach[47] to investigate an allosteric effect and compare the catalytic impact of active site conformational change traverses a challenge in the field, as recently noted by Himo and de Visser.[48,49]

RESULTS AND DISCUSSION

Active Site Models

Positions of the active site residues and the Gln substrate are highly conserved in crystallographic models except for the HisFH dimer conformation composed of chains E and F from PDB 7ac8 (Figure 2). There are four distinct geometric differences observed in this conformation: 1) an interfacial residue, *f*Gln123, interacts with the bound Gln as a result of subunit closure; 2) the *h*Val51 amide N–H points toward the substrate carbonyl; 3) the oxyanion strand is positioned above the catalytic thiol; and 4) the reactive carboxamide of Gln is preorganized for acylation.

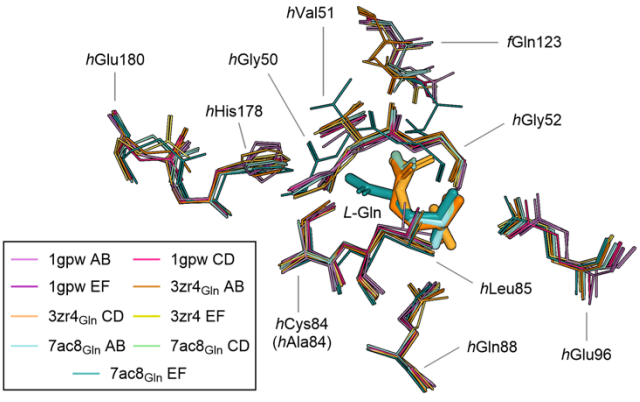

Figure 2. Overlap of HisH active-site geometries across multiple crystallized structures.

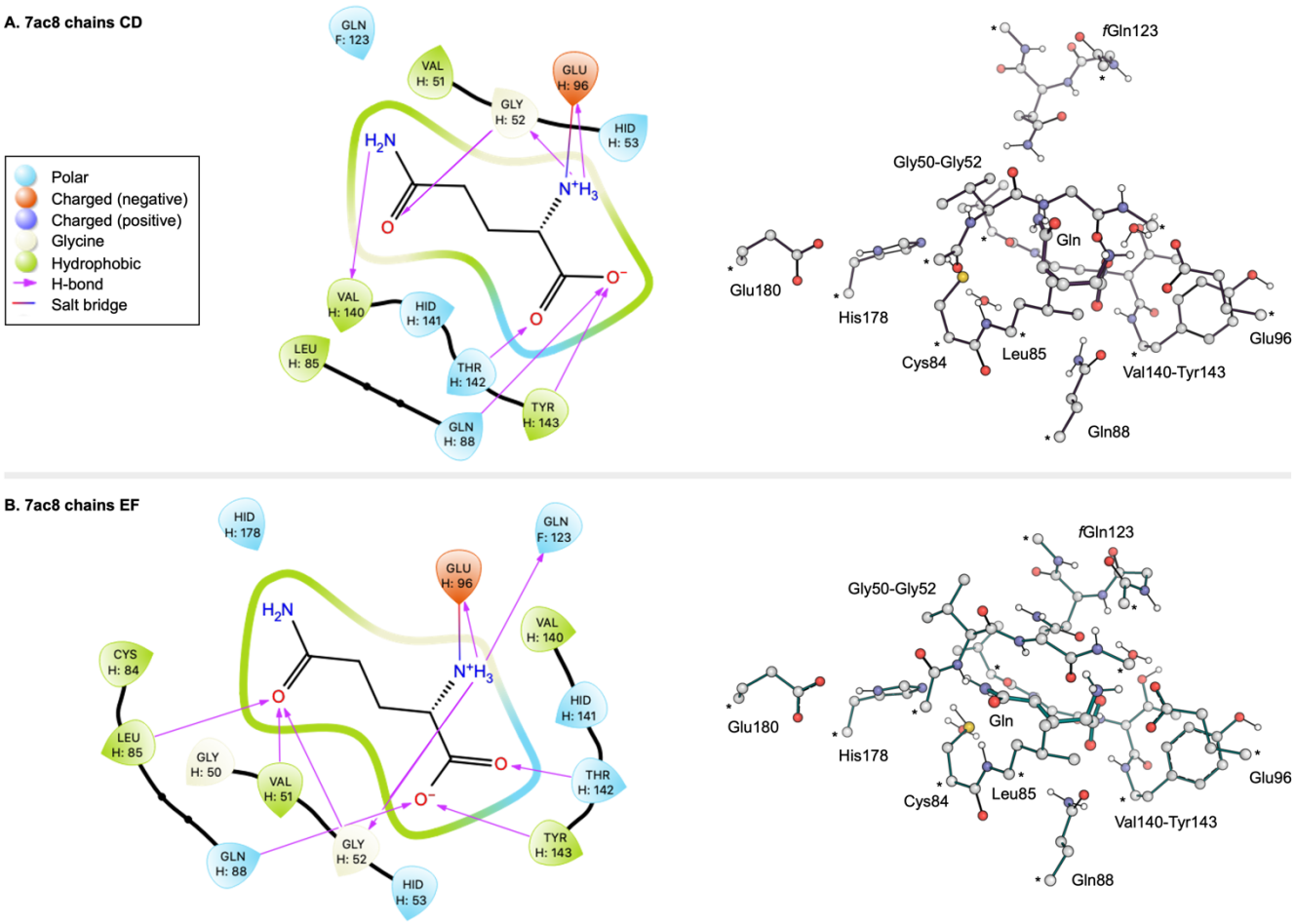

Figure 3. Interactions at the HisH active site in the inactive (left-top) and active (left-bottom) conformations and resulting QM cluster models (right). Asterisks indicate Cα atoms frozen during geometry optimizations.

Two truncated active site models were created from the 7ac8[14] crystallized unit of IGPS using atomic positions from chains E/F and chains C/D; the deposition authors refer to these complexes as active and inactive conformations, respectively. Residue *h*Ala84 in chains F and D was reverted back to wild-type *h*Cys84 with PyMol[50] by selecting the backbone-dependent side chain rotamer with the least steric clash. We will refer to these truncated models as Active and Inactive.

The size and residue components of the QM model are important to consider, and informed decisions based on selection criteria remain an active area of development.[51–56] Residues were selected based on interactions (Fig. 3) with the substrate and biochemical relevance indicated in the literature. The ligand interaction diagrams in Figure 3 illustrate how the C/D and E/F conformations yield different interactions with the glutamine substrate. Since the main objective of this work is to evaluate the catalytic impact of active site structural changes, we focused on building models suitable for direct comparison. Therefore, the same atoms were included in each model from the following residues: *f*Gly121, *f*Ser122, *f*Gln123 and *f*Ala124 from the HisF subunit, *h*Gly50, *h*Val51, *h*Gly52, *h*His53, *h*Cys84, *h*Leu85, *h*Gln88, *h*Glu96, *h*Val140, *h*His141, *h*Thr142, *h*Tyr143, *h*His178 and *h*Glu180 from the HisH subunit, the Gln substrate in zwitterionic form and two conserved crystallographic waters. Hereon, all residues without a prefix are assumed to be from the HisH monomer since they are the model majority, but the HisF prefix will be kept for clarity. Amino acid side and main chains were truncated according to potential involvement in the elementary reaction steps and interactions with the substrate (see Table S1 and text for a detailed list of included atoms, truncation scheme, and geometry optimization constraints). Each model contains 237 atoms, an overall charge of –2 and 12 constrained carbon atoms (Figure 3). Geometry optimizations were performed with the range-separated, dispersion-corrected ωB97X-D[64] functional using the 6-31G*[65] basis set for all C, H, and N atoms and the 6-31+G*[66] basis set for S and O atoms. Stationary point electronic energies were further refined at the B3LYP-D3(BJ)/6-311+G(2d,2p) level of theory and the default IEF–PCM implicit solvent method with internal parameters for diethyl ether (ε=4.24).[67–72] Additional information is presented in the Computational Details section.

Acylation Reaction Mechanism

The thioester formation mechanism proposed in this work (Figure 4) begins from the enzyme-substrate (**ES**) complex with deprotonation of Cys84 by His178 to form the thiolate in **Int1**. The nucleophilic Cys84 attacks the substrate carbonyl forming a tetrahedral oxyanion intermediate (**Int2**). The His178 imidazolium transfers a proton to the substrate to form an ammonium in (**Int3**). Lastly, the tetrahedral

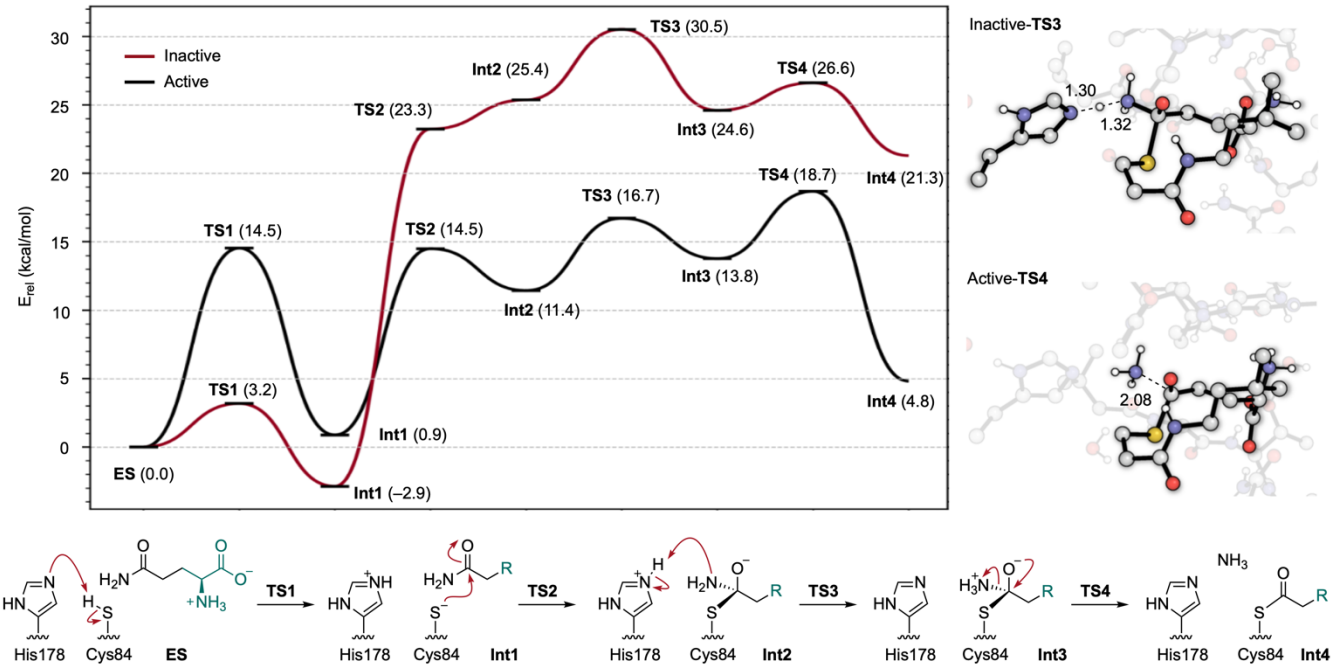

Figure 4. Energy profiles of Active (black) and Inactive (red) IGPS active site geometries showing ΔE relative to each model's enzyme substrate (**ES**) complex in kcal/mol. Representations of the rate-limiting steps corresponding to each model with TS bonds shown as dotted lines and distances in Å.

intermediate collapses and the N–C bond breaks, forming the thioester acyl-intermediate and liberating ammonia (**Int4**). All optimized structures are shown in the SI.

The electronic energy profiles of Active and Inactive models (Figure 4) illustrate how differences in active site geometry substantially influence the reaction. Deprotonation of Cys84 in Active has a barrier of 14.5 kcal/mol, significantly higher than the 3.2 kcal/mol required for Inactive. This difference is due to the positioning of the Gln substrate. In the optimized Active-**ES**, the substrate is observed in a near-attack conformation, with the carbonyl carbon 3.56 Å from the Cys84 sulfur and the NH_2 group hydrogen bonding with the His178 Nε (2.01 Å). This interaction is disrupted in the Active-**TS1** when the His178 Nε accepts the proton from Cys84. Alternatively, in the Inactive-**ES** the substrate is positioned farther away (3.84 Å), which enables Cys84 to hydrogen bond with His178 (1.91 Å). The Gln pose optimized in Inactive is not possible in Active because the proximity of *f*Gln123 confines the substrate.

The rate of thioester formation in the Active geometry is determined by the collapse of the tetrahedral oxyanion intermediate, with a TS bond breaking distance of 2.08 Å (Active-**TS4**, Figure 4). This yields a computationally predicted barrier of $\Delta E^{\ddagger}$=18.7 kcal/mol, which agrees well with the experimental rate of *T. maritima* (0.67 ± 0.02 s^{-1} at 298.15 K, corresponding to a barrier of around 17.7 kcal/mol).[6] Isotope effects of the amide nitrogen on glutamine bound to a similar class-I GAT, carbamyl phosphate synthetase (CPS), support the release of ammonia as the rate-limiting step.[11] Thioester formation was also found to be rate-limiting in cysteine esterase.[57]

In the Inactive geometry, the formation of ammonium (Inactive-**TS3**, Figure 4) is highest in energy, yielding a barrier of $\Delta E^{\ddagger}$=30.5 kcal/mol for thioester formation. This barrier is larger than experimental measurements (21.1 and 22.7 kcal/mol).[6,58] Alternative mechanistic pathways were explored, such as concerted NH_3 formation and tetrahedral collapse, but were not located. Another possibility is that more energetically favorable structural rearrangements occur along the reaction coordinate to enable catalysis. In support of this, the barrier for the Val51 backbone flip in the absence of PrFAR is estimated by steered MD to be approximately 22 kcal/mol,[35] which aligns well with the experimental rate. Therefore, our current DFT results suggest that the enzymatic reaction rate in the absence of the allosteric effector is limited by the barrier for conformational interconversion rather than by the elementary bond-forming and breaking steps in the active site.

The elementary step most affected by an active site structural change is the formation of the tetrahedral acyl-enzyme via **TS2**. This transformation requires 13.6 kcal/mol from **Int1** in Active and nearly twice as much in Inactive (26.1 kcal/mol). This step demonstrates the importance of IGPS active site geometry in stabilizing the incipient oxyanion. Although it has been proposed that the IGPS structure 3zr4 (structurally consistent with our Inactive model) is in a catalytically competent conformation with the Gly52 N–H completing the oxyanion hole, our data instead indicate that the energy associated with the Inactive geometry hinders thioester formation.

There are multiple structural differences between Active and Inactive models. These include the Val51 backbone flip and *f*Gln123 proximity, but also less apparent variations, such as the relative position of the oxyanion strand (Figure S1). The capacity of Gly52 to serve as an H-bond donor along the reaction coordinate may depend on the subtle positioning of the oxyanion strand. Additionally, it is unclear from the energy profiles alone how proximity of *f*Gln123

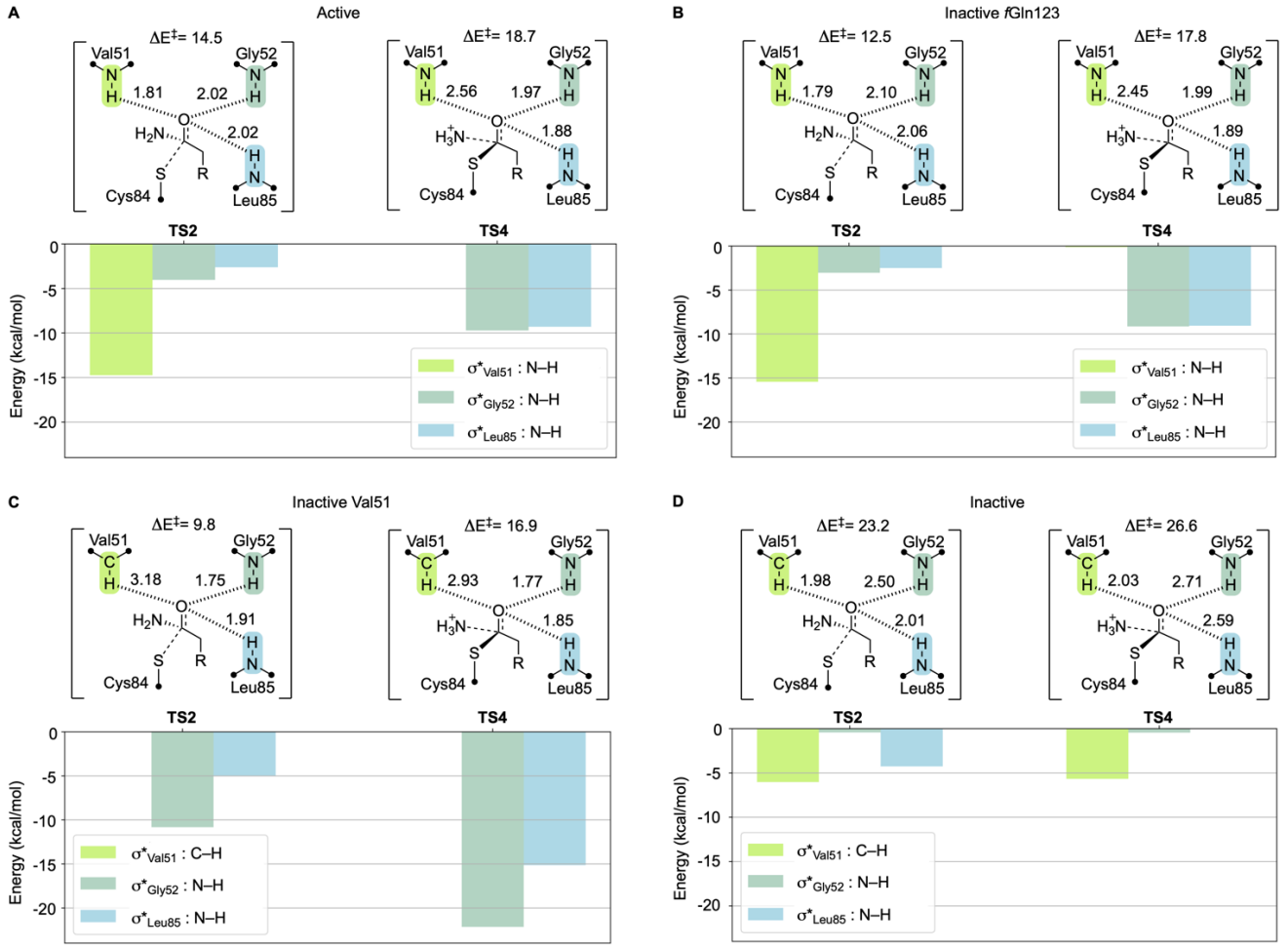

Figure 5. Energetic contributions to oxyanion stabilization during oxyanion formation (**TS1**) and oxyanion collapse (**TS3**) measured by NBO[59] analysis. Top quadrants A and B correspond to models with the Val51 N-H pointing into the active site: Active and Inactive *f*Gln123. Bottom quadrants C and D correspond to models with the Val51 N-H directed outwards: Inactive Val51 and Inactive.

influences the reaction. We therefore pursued additional computational studies to deconvolute the energetic effects due to specific structural variations in the IGPS acylation reaction.

Oxyanion Hole Contributions

Two additional models, Inactive *f*Gln123 and Inactive Val51, were manually constructed (see SI for construction details) to analyze separately how *f*Gln123 proximity, the Val51 backbone conformation, and the position of the oxyanion strand influence TS stabilization in the Active model. This approach is reminiscent of theozyme modeling,[60] where residues, or functional groups, are hypothetically arranged in a truncated active site to explore catalytic contributions of individual atomic interactions and predict optimal catalytic scaffolds. In our approach, the distinct models enable us to quantify the influence of each structural difference relative to the active model separately. The oxyanion hole contributions were evaluated in each TS by estimating the donor-acceptor orbital interaction energies of the Leu85, Gly52 and Val51 σ^* orbitals and the Gln Oε lone pair electrons via Natural Bonding Orbital (NBO) analysis.[59] Calculation details are found in the Computational Details section.

As hypothesized, the Active oxyanion hole structure provides substantial stabilization (Figure 5A). Val51 is the predominant stabilizing component during oxyanion formation (**TS2**), with a favorable interaction energy of –14.7 kcal/mol. Contributions from Gly52 and Leu85 are much smaller (–4.0 kcal/mol and –2.6 kcal/mol, respectively). Surprisingly, when the oxyanion species breaks down in **TS4**, Val51 no longer interacts with the oxyanion. The N–H shifts direction to interact with the lone pair of electrons on the His178 Nε. To ensure the Active-**TS4** geometry optimization was not unintentionally biased by the initial geometry input, the oxyanion strand fragment in the optimized **TS4** structure was replaced with that from the optimized **TS2** structure. The optimization converged to the same **TS4** structure, suggesting this is the appropriate first-order saddle point.

Although the Val51 N–H points away from the active site in the Inactive model, the Val51 Cα–H stabilizes **TS2** by –5.9 kcal/mol and **TS4** by –4.9 kcal/mol (Figure 5D). Leu85 contributes –4.3 kcal/mol in Inactive-**TS2**, which is slightly more than its contributions in Active-**TS2** and Inactive *f*Gln123-**TS2** (Figure 5B), presumably to compensate for the weak interaction from Val51. However, during oxyanion breakdown in Inactive-**TS4**, the Gln:Oε–Leu85:H distance extends to 2.59 Å, resulting in no appreciable stabilization.

Inactive Val51 differs from Active only in the backbone dihedrals of Val51; the N–H points away from the active site, mimicking the inactive conformation, but the oxyanion strand position is consistent with Active. The Gly52 N–H contributes –10.8 kcal/mol in Inactive Val51-**TS2,** which is less than the contributions from Val51 in Active (–14.7 kcal/mol), but the difference in energy between **TS2** and **ES** in Inactive Val51 is smaller ($\Delta E^{\ddagger}$=9.8 kcal/mol, vs. ($\Delta E^{\ddagger}$=14.5 kcal/mol in Active) (Figure 5C). This results from a higher energy Inactive Val51-**ES** relative to Active-**ES** (ΔE=5.3 kcal/mol), while the **TS2** structures have approximately the same energy (ΔE=0.7 kcal/mol). The atom positions frozen during geometry optimizations are the same between Inactive Val51 and Active; therefore, their structure energies can be directly compared, unlike the other models. The Inactive Val51 oxyanion hole stabilizes **TS4** more than in any other model (nearly twice that of Active-**TS4**). This is because a third lone pair of electrons is detected in the NBO analysis of this structure, whereas the other structures only have two electron lone pairs in **TS4**. Regardless, Inactive Val51-**TS4** is 3.4 kcal/mol higher in energy than Active-**TS4**, consistent with less efficient catalysis than in the Active construct.

In the initial Inactive Val51 model, the Val51 φ dihedral matches that of the optimized Inactive-**ES** structure (–138°) by construction. During geometry optimizations, the dihedral adjusts to –111° in Inactive Val51. This adjustment is consistent with the description of a third oxyanion strand conformation identified in MD simulations as an intermediate conformation of the Val51 dihedral flip.[35] The partial dihedral rotation introduces a weak interaction (less than 0.5 kcal/mol) between the Gln Oε lone pair electrons and the π* orbital of backbone Gly50 C=O. This type of n–π* interaction to stabilize an oxyanion tetrahedral intermediate has precedence in aspartic proteases[61] and, therefore, could be a catalytically relevant state in IGPS.

Although Gly52 does not contribute to oxyanion stabilization in the inactive conformation, as previously suggested, [41] repositioning of the oxyanion strand enables such stabilizing interactions, as shown in the Inactive Val51 model. In addition, the new crystallographic conformation of IGPS (7ac8 chains E/F) also results in a catalytically competent oxyanion hole geometry involving Val51. From the energetic perspective both the Active and Inactive Val51 models are consistent with experimental kinetic data.

Decomposition of *f*Gln123 Interaction Energy

The proximity of *f*Gln123 to the HisH active site is another structural feature influenced by the binding of the allosteric effector, PrFAR. It is expected that *f*Gln123 assists in recruiting and stabilizing the glutamine substrate, but it is unclear to what extent, if any, this proximity influences the chemical coordinate. The Inactive *f*Gln123 oxyanion hole contributions (Figure 5B) are nearly identical to Active, with an average difference of less than 0.2 kcal/mol per residue in each TS (all numerical values are listed in Table S2). Therefore, the oxyanion hole energetics are not influenced by the proximity of *f*Gln123.

To further investigate the role of *f*Gln123, the interaction energy between *f*Gln123 and the HisH active site is calculated via the ALMO–EDA procedure for each QM model (Computational Methods). The total interaction energy (Total INT) in **ES** is much more favorable when *f*Gln123 is closer to the active site. Active- and Inactive Val51-ES have similar *f*Gln123 interaction energies of –29.2 and –30.6 kcal/mol, which are much lower than the Inactive *f*Gln123 and Inactive values (–5.4 and –13.1 kcal/mol, respectively) (Figure 6). The difference in *f*Gln123 interaction energy between Inactive *f*Gln123 and Inactive can be reasoned by the presence of a hydrogen bond between the sidechain NH_2 group of *f*Gln123 and the backbone carbonyl oxygen of Val140 (Figure S4) that is present in the Inactive model but absent in the Inactive *f*Gln123model.

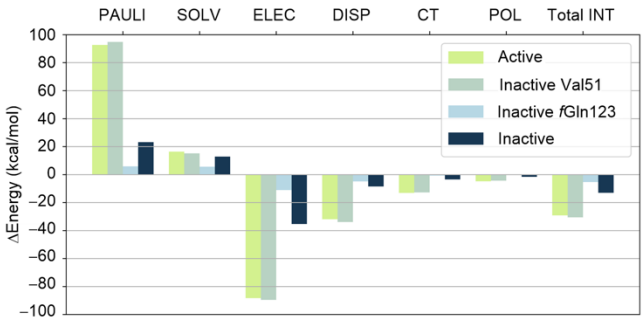

Figure 6. Decomposition of interaction energy calculated with ALMO-EDA between *f*Gln123 and the HisH active site in the optimized **ES** complex for each QM model.

The interaction energy in Inactive Val51 becomes slightly less favorable in **TS2**, **TS3**, and **TS4** because the Gly52 backbone shifts away from *f*Gln123 to interact more strongly with the Gln Oε. The Inactive model also shows interaction energy changes between **ES** and **TS2**, **TS3**, and **TS4**, because the Gln substrate moves farther from *f*Gln123 to react with Cys84. The Active and Inactive *f*Gln123 models have minimal structural rearrangements along the reaction coordinate; therefore, the *f*Gln123 interaction energy values are consistent across the evaluated structures.

CONCLUSIONS

This work provides new insights into local active site structural changes that yield energetics consistent with experimentally measured allosteric rate acceleration in IGPS. The hypothesized Val51 backbone flip leads to a more favorable reaction pathway via oxyanion hole stabilization, supporting the longstanding hypothesis to explain the observed allosteric effect. However, this work reveals that this is not the only plausible configuration to yield the expected catalytic effect, as the Gly52 N–H is also a capable oxyanion hole contributor.

Oxyanion stabilization via Gly52 has been proposed previously,[41] however, most studies to date have focused on the Val51 dihedral flip. When the Val51 backbone of the Active model is manually modified to mimic the Inactive structure the Gly52 N–H becomes a suitable oxyanion hole donor. These results show that multiple active site conformations are catalytically competent and reveal the positioning of the oxyanion strand is a definitive structural change required for proper oxyanion hole formation.

Two other class-I GATs, pyridoxal 5'-phosphate (PLP, PDB: 2NV2[30]) synthase and carbamoyl phosphate synthetase (CPS, PDB: 1C3O[62]), have been crystallized in their catalytic forms with the Gln substrate bound. Upon alignment of the Gln substrate reactive carboxamide, the oxyanion strand residue involved in the preformed oxyanion holes in PLP synthase and CPS is more structurally consistent with the IGPS Gly52 than Val51 in Active-**ES**. Alignment with Inactive Val51-**ES** shows an even closer alignment, providing evidence that this manually constructed geometry of the IGPS glutaminase active site is feasible. Lastly, glutaminase activation via oxyanion strand repositioning has been proposed for another class-I GAT, aminodeoxychorismate synthase (ADCS), which displays an allosteric response similar to IGPS.[42] Cumulatively, these data are consistent with the computed mechanism and transition structures put forward here.

The truncated active-site approach uniquely allowed for the modification of distinct structural features. Such modifications would be inaccessible or much more challenging with alternative modeling approaches (e.g., QM/MM) that explicitly treat the protein environment. This approach is generalizable to other systems in efforts to probe the energetic influence of local structural aspects and highlights the unique applications available to theozyme and cluster modeling.

Computational Details

Geometry optimizations were performed using Gaussian 16, Revision C.01[63] with the range-separated, dispersion-corrected ωB97X-D[64] functional using the 6-31G*[65] basis set for all C, H, and N atoms and the 6-31+G*[66] basis set for S and O atoms. The α-carbons of selected protein residues were frozen during optimizations to conserve the active site geometry in the absence of the greater protein environment. All geometries were inspected for structural distortions that could have occurred during optimization. Vibrational frequencies were computed to confirm the nature of minima (all real normal modes) and transition structures (a single imaginary normal mode). Stationary point electronic energies were further refined at the B3LYP-D3(BJ)/6-311+G(2d,2p) level of theory and the default IEF–PCM implicit solvent method with internal parameters for diethyl ether (ε=4.24).[67–72] This procedure is commonly applied in enzymatic QM cluster modeling.[47,73,74] The GoodVibes software was used to generate electronic energy profiles.[75] The energetic span[76] between the lowest energy intermediate and the highest energy transition structure (TS) was used to estimate the activation energy. Due to the necessary frozen constraints during geometry optimizations, the vibrational partition function is not considered reliable. Therefore, we focus on the electronic energy profile (i.e., rather than Gibbs energy) throughout. This approximation is common in truncated enzyme modeling and has shown success in mechanistic investigations.

The oxyanion hole strength in **TS2**, **TS3**, and **TS4** of every model was assessed using the Natural Bond Orbital (NBO) analysis program (version 7.0.5)[59]. NBO analysis transforms the optimized atomic orbital basis set into a localized, ideal Lewis structure basis. Second-order perturbation theory analysis of the Fock matrix in the NBO basis is used to estimate the stabilization energy associated with electron delocalization from a filled donor NBO to an unfilled acceptor NBO. The default interaction energy minimum threshold of 0.05 kcal/mol was used. The oxyanion hole interaction energies were investigated between Gln Oε lone pair electrons and the σ* orbitals of the backbone N–H of Leu85, Gly52, and Val51. Additionally, the Val51 Cα–H was investigated in Inactive Val51 and Inactive.

To better understand how *f*Gln123 influences the pathway energetics, we evaluated the interaction energy between the *f*Gln123 molecular fragment and the rest of the active site residues for the Active, Inactive *f*Gln123, Inactive Val51 and Inactive models. Absolutely Localized Molecular Orbitals based Energy Decomposition Analysis (ALMO–EDA) implemented in Q–Chem 5.4 was performed at the B3LYP-D3(BJ)/6-311+G(2d,2p) level of theory and CPCM with ε=4.24, to be consistent with the single-point energies used to produce the reaction profiles.[77,78] Within this framework, the interaction energy is defined as:

$\Delta E_{INT} = \Delta E_{FRZ} + \Delta E_{POL} + \Delta E_{CT}$.

E_{POL} and E_{CT} refer to the polarization and charge transfer energy components, respectively. The E_{FRZ} term combines the interaction energy contributions of the unrelaxed fragment densities, namely attractive dispersion (E_{DISP}), repulsive Pauli (E_{PAULI}) and permanent electrostatics (E_{ELEC}):

$\Delta E_{FRZ} = \Delta E_{DISP} + \Delta E_{PAULI} + \Delta E_{ELEC}$.

ASSOCIATED CONTENT

The Supporting Information is available free of charge with information on IGPS active site model components and protonation states, construction of the Inactive Val52 and Inactive fGln123 models, NBO calculation details, ALMO-EDA calculation details, absolute energies from geometry optimizations and single point corrects for all evaluated structures, Geometries and relevant atomic distances of each evaluated transition state, and structural comparisons with PLP synthase.

Raw data of all calculations and the corresponding software keywords and versions, aligned xyz coordinates of all evaluated structures, and the energy profiles of the Active and Inactive models calculated with 1) ωB97X-D/6-31G*(C,H,N);6-31+G*(S,O) 2) ωB97X-D/def2QZVPP and 3) B3LYP-D3(BJ)/6-311+G(2d,2p), are publicly accessible at https://github.com/hklem/IGPS_QM_cluster_models.

AUTHOR INFORMATION

Corresponding Author

Heidi Klem – *Department of Chemistry, Colorado State University, Fort Collins, Colorado 80523, United States*; orcid.org/0000-0002-9604-1709;
Email: Heidi.Klem@colostate.edu

Juan V. Alegre-Requena – Departamento de Química Inorgánica, Instituto de Síntesis Química y Catálisis Homogénea (ISQCH) CSIC-Universidad de Zaragoza, Zaragoza 50009, Spain; orcid.org/0000-0002-0769-7168;
Email: jv.alegre@csic.es

Robert S. Paton – *Department of Chemistry, Colorado State University, Fort Collins, Colorado 80523, United States*; orcid.org/0000-0002-0104-4166;
Email: Robert.Paton@colostate.edu

Author Contributions

All authors have approved the final version of the manuscript.

Funding Sources

J.V.A.-R. thanks the Red Española de Supercomputación (grant number QH-2023-1-0003), the Gobierno de Aragón-Fondo Social Europeo (Research Groups E07_23R), and the Ministry of Science and Innovation (MCIN) for a Juan de la Cierva Incorporación contract under grant reference IJC2020-044217-I. R.S.P. acknowledges support from the National Science Foundation (NSF CHE1955876) and computational resources from the RMACC Summit supercomputer supported by the NSF (ACI-1532235 and ACI-1532236), the University of Colorado Boulder and Colorado State University, and ACCESS through allocation TG-CHE180056.

Notes

The authors declare no competing financial interest.

ACKNOWLEDGMENT

J.V.A.-R. acknowledges the computing resources at the Galicia Supercomputing Center, CESGA, including access to the Finis-Terrae supercomputer and the Drago cluster facility of SGAI-CSIC.

REFERENCES

(1) Klem, T. J.; Davisson, V. J. Imidazole Glycerol Phosphate Synthase: The Glutamine Amidotransferase in Histidine Biosynthesis. *Biochemistry* **1993**, *32* (19), 5177–5186.
(2) Beismann-Driemeyer, S.; Sterner, R. Imidazole Glycerol Phosphate Synthase fromThermotoga Maritima. *J. Biol. Chem.* **2001**, *276* (23), 20387–20396.
(3) Massière, F.; Badet-Denisot, M.-A. The Mechanism of Glutamine-Dependent Amidotransferases. *Cell. Mol. Life Sci.* **1998**, *54* (3), 205–222.
(4) Zalkin, H.; Smith, J. L. Enzymes Utilizing Glutamine as an Amide Donor. In *Advances in Enzymology - and Related Areas of Molecular Biology*; Purich, D. L., Ed.; John Wiley & Sons, Inc.: Hoboken, NJ, USA, 1998; pp 87–144.
(5) Douangamath, A.; Walker, M.; Beismann-Driemeyer, S.; Vega-Fernandez, M. C.; Sterner, R.; Wilmanns, M. Structural Evidence for Ammonia Tunneling across the (B/a)8 Barrel of the Imidazole Glycerol Phosphate Synthase Bienzyme Complex. *Structure* **2002**, *10*, 185–193.
(6) Kneuttinger, A. C.; Rajendran, C.; Simeth, N. A.; Bruckmann, A.; König, B.; Sterner, R. Significance of the Protein Interface Configuration for Allostery in Imidazole Glycerol Phosphate Synthase. *Biochemistry* **2020**, *59* (29), 2729–2742.
(7) Smith, A. J. T.; Müller, R.; Toscano, M. D.; Kast, P.; Hellinga, H. W.; Hilvert, D.; Houk, K. N. Structural Reorganization and Preorganization in Enzyme Active Sites: Comparisons of Experimental and Theoretically Ideal Active Site Geometries in the Multistep Serine Esterase Reaction Cycle. *J. Am. Chem. Soc.* **2008**, *130* (46), 15361–15373.
(8) Ma, S.; Devi-Kesavan, L. S.; Gao, J. Molecular Dynamics Simulations of the Catalytic Pathway of a Cysteine Protease: A Combined QM/MM Study of Human Cathepsin K. *J. Am. Chem. Soc.* **2007**, *129* (44), 13633–13645.
(9) Chittur, S. V.; Klem, T. J.; Shafer, C. M.; Davisson, V. J. Mechanism for Acivicin Inactivation of Triad Glutamine Amidotransferases. *Biochemistry* **2001**, *40* (4), 876–887.
(10) Thoden, J. B.; Miran, S. G.; Phillips, J. C.; Howard, A. J.; Raushel, F. M.; Holden, H. M. Carbamoyl Phosphate Synthetase: Caught in the Act of Glutamine Hydrolysis. *Biochemistry* **1998**, *37*, 8825--8831.
(11) Rishavy, M. A.; Cleland, W. W.; Lusty, C. J. ^{15} N Isotope Effects in Glutamine Hydrolysis Catalyzed by Carbamyl Phosphate Synthetase: Evidence for a Tetrahedral Intermediate in the Mechanism. *Biochemistry* **2000**, *39* (24), 7309–7315.
(12) Pina, A. F.; Sousa, S. F.; Cerqueira, N. M. F. S. A. The Catalytic Mechanism of Pdx2 Glutaminase Driven by a Cys-His-Glu Triad: A Computational Study. *ChemBioChem* **2022**, *23* (9).
(13) van den Heuvel, R. H. H.; Curti, B.; Vanoni, M. A.; Mattevi, A. Glutamate Synthase: A Fascinating Pathway from L-Glutamine to L-Glutamate. *Cell. Mol. Life Sci.* **2004**, *61* (6), 669–681.
(14) Wurm, J. P.; Sung, S.; Kneuttinger, A. C.; Hupfeld, E.; Sterner, R.; Wilmanns, M.; Sprangers, R. Molecular Basis for the Allosteric Activation Mechanism of the Heterodimeric Imidazole Glycerol Phosphate Synthase Complex. *Nat. Commun.* **2021**, *12* (1), 2748.
(15) List, F.; Bocola, M.; Haeger, M. C.; Sterner, R. Constitutively Active Glutaminase Variants Provide Insights into the Activation Mechanism of Anthranilate Synthase. *Biochemistry* **2012**, *51* (13), 2812–2818.
(16) VanWart, A. T.; Eargle, J.; Luthey-Schulten, Z.; Amaro, R. E. Exploring Residue Component Contributions to Dynamical Network Models of Allostery. *J. Chem. Theory Comput.* **2012**, *8* (8), 2949–2961.
(17) Ribeiro, A. A. S. T.; Ortiz, V. Determination of Signaling Pathways in Proteins through Network Theory: Importance of the Topology. *J. Chem. Theory Comput.* **2014**, *10* (4), 1762–1769.
(18) Van Wart, A. T.; Durrant, J.; Votapka, L.; Amaro, R. E. Weighted Implementation of Suboptimal Paths (WISP): An Optimized Algorithm and Tool for Dynamical Network Analysis. *J. Chem. Theory Comput.* **2014**, *10* (2), 511–517.
(19) Negre, C. F. A.; Morzan, U. N.; Hendrickson, H. P.; Pal, R.; Lisi, G. P.; Loria, J. P.; Rivalta, I.; Ho, J.; Batista, V. S. Eigenvector Centrality for Characterization of Protein Allosteric Pathways. *Proc. Natl. Acad. Sci.* **2018**, *115* (52).
(20) Botello-Smith, W. M.; Luo, Y. Robust Determination of Protein Allosteric Signaling Pathways. *J. Chem. Theory Comput.* **2019**, *15* (4), 2116–2126.
(21) Gheeraert, A.; Pacini, L.; Batista, V. S.; Vuillon, L.; Lesieur, C.; Rivalta, I. Exploring Allosteric Pathways of a V-Type Enzyme with Dynamical Perturbation Networks. *J. Phys. Chem. B* **2019**, *123* (16), 3452–3461.
(22) Lake, P. T.; Davidson, R. B.; Klem, H.; Hocky, G. M.; McCullagh, M. Residue-Level Allostery Propagates through the Effective Coarse-Grained Hessian. *J. Chem. Theory Comput.* **2020**, *16* (5), 3385–3395.
(23) Maschietto, F.; Gheeraert, A.; Piazzi, A.; Batista, V. S.; Rivalta, I. Distinct Allosteric Pathways in Imidazole Glycerol Phosphate Synthase from Yeast and Bacteria. *Biophys. J.* **2022**, *121* (1), 119–130.

(24) Yao, X.-Q.; Hamelberg, D. Residue–Residue Contact Changes during Functional Processes Define Allosteric Communication Pathways. *J. Chem. Theory Comput.* **2022**, *18* (2), 1173–1187.
(25) Lipchock, J. M.; Loria, J. P. Nanometer Propagation of Millisecond Motions in V-Type Allostery. *Structure* **2010**, *18* (12), 1596–1607.
(26) Rivalta, I.; Sultan, M. M.; Lee, N.-S.; Manley, G. A.; Loria, J. P.; Batista, V. S. Allosteric Pathways in Imidazole Glycerol Phosphate Synthase. *Proc. Natl. Acad. Sci.* **2012**, *109* (22).
(27) Lisi, G. P.; Manley, G. A.; Hendrickson, H.; Rivalta, I.; Batista, V. S.; Loria, J. P. Dissecting Dynamic Allosteric Pathways Using Chemically Related Small-Molecule Activators. *Structure* **2016**, *24* (7), 1155–1166.
(28) Knöchel, T.; Ivens, A.; Hester, G.; Gonzalez, A.; Bauerle, R.; Wilmanns, M.; Kirschner, K.; Jansonius, J. N. The Crystal Structure of Anthranilate Synthase from *Sulfolobus Solfataricus* : Functional Implications. *Proc. Natl. Acad. Sci.* **1999**, *96* (17), 9479–9484.
(29) Tesmer, J. J. G.; Klem, T. J.; Deras, M. L.; Davisson, V. J.; Smith, J. L. The Crystal Structure of GMP Synthetase Reveals a Novel Catalytic Triad and Is a Structural Paradigm for Two Enzyme Families. *Nat. Struct. Biol.* **1996**, *3* (1), 74–86.
(30) Strohmeier, M.; Raschle, T.; Mazurkiewicz, J.; Rippe, K.; Sinning, I.; Fitzpatrick, T. B.; Tews, I. Structure of a Bacterial Pyridoxal 5′-Phosphate Synthase Complex. *Proc. Natl. Acad. Sci.* **2006**, *103* (51), 19284–19289.
(31) Morar, M.; Hoskins, A. A.; Stubbe, J.; Ealick, S. E. Formylglycinamide Ribonucleotide Amidotransferase from *Thermotoga Maritima:* Structural Insights into Complex Formation. *Biochemistry* **2008**, *47* (30), 7816–7830.
(32) Hongmin, L.; Ryan, T. J.; Chave, K. J.; Van Roey, P. Three-Dimensional Structure of Human -Glutamyl Hydrolase. *J. Biol. Chem.* **2002**, *277* (27), 24522–24529.
(33) Rivalta, I.; Lisi, G. P.; Snoeberger, N.-S.; Manley, G.; Loria, J. P.; Batista, V. S. Allosteric Communication Disrupted by a Small Molecule Binding to the Imidazole Glycerol Phosphate Synthase Protein–Protein Interface. *Biochemistry* **2016**, *55* (47), 6484–6494.
(34) Lipchock, J.; Loria, J. P. Millisecond Dynamics in the Allosteric Enzyme Imidazole Glycerol Phosphate Synthase (IGPS) from Thermotoga Maritima. *J. Biomol. NMR* **2009**, *45* (1–2), 73–84.
(35) Calvó-Tusell, C.; Maria-Solano, M. A.; Osuna, S.; Feixas, F. Time Evolution of the Millisecond Allosteric Activation of Imidazole Glycerol Phosphate Synthase. *J. Am. Chem. Soc.* **2022**, *144* (16), 7146–7159.
(36) Myers, R. S.; Amaro, R. E.; Luthey-Schulten, Z. A.; Davisson, V. J. Reaction Coupling through Interdomain Contacts in Imidazole Glycerol Phosphate Synthase. *Biochemistry* **2005**, *44* (36), 11974–11985.
(37) Chaudhuri, B. N.; Lange, S. C.; Myers, R. S.; Davisson, V. J.; Smith, J. L. Toward Understanding the Mechanism of the Complex Cyclization Reaction Catalyzed by Imidazole Glycerol Phosphate Synthase: Crystal Structures of a Ternary Complex and the Free Enzyme. *Biochemistry* **2003**, *42* (23), 7003–7012.
(38) Myers, R. S.; Jensen, J. R.; Deras, I. L.; Smith, J. L.; Davisson, V. J. Substrate-Induced Changes in the Ammonia Channel for Imidazole Glycerol Phosphate Synthase. *Biochemistry* **2003**, *42* (23), 7013–7022.
(39) Chaudhuri, B. N.; Lange, S. C.; Myers, R. S.; Chittur, S. V.; Davisson, V. J.; Smith, J. L. Crystal Structure of Imidazole Glycerol Phosphate Synthase: A Tunnel through a (β/α)8 Barrel Joins Two Active Sites. *Structure* **2001**, *10*, 987--997.
(40) Korolev, S.; Skarina, T.; Evdokimova, E.; Beasley, S.; Edwards, A.; Joachimiak, A.; Savchenko, A. Crystal Structure of Glutamine Amidotransferase fromThermotoga Maritima. *Proteins Struct. Funct. Genet.* **2002**, *49* (3), 420–422.
(41) List, F.; Vega, M. C.; Razeto, A.; Häger, M. C.; Sterner, R.; Wilmanns, M. Catalysis Uncoupling in a Glutamine Amidotransferase Bienzyme by Unblocking the Glutaminase Active Site. *Chem. Biol.* **2012**, *19* (12), 1589–1599.
(42) Semmelmann, F.; Straub, K.; Nazet, J.; Rajendran, C.; Merkl, R.; Sterner, R. Mapping the Allosteric Communication Network of Aminodeoxychorismate Synthase. *J. Mol. Biol.* **2019**, *431* (15), 2718–2728.
(43) Klem, H.; McCullagh, M.; Paton, R. S. Modeling Catalysis in Allosteric Enzymes: Capturing Conformational Consequences. *Top. Catal.* **2022**, *65* (1–4), 165–186.
(44) Glowacki, D. R.; Harvey, J. N.; Mulholland, A. J. Taking Ockham's Razor to Enzyme Dynamics and Catalysis. *Nat. Chem.* **2012**, *4* (3), 169–176.
(45) Ryde, U. How Many Conformations Need To Be Sampled To Obtain Converged QM/MM Energies? The Curse of Exponential Averaging. *J. Chem. Theory Comput.* **2017**, *13* (11), 5745–5752.
(46) Masgrau, L.; Truhlar, D. G. The Importance of Ensemble Averaging in Enzyme Kinetics. *Acc. Chem. Res.* **2015**, *48* (2), 431–438.
(47) Siegbahn, P. E. M.; Himo, F. The Quantum Chemical Cluster Approach for Modeling Enzyme Reactions. *Wiley Interdiscip. Rev. Comput. Mol. Sci.* **2011**, *1* (3), 323–336.
(48) Himo, F.; de Visser, S. P. Status Report on the Quantum Chemical Cluster Approach for Modeling Enzyme Reactions. *Commun. Chem.* **2022**, *5* (1), 29.
(49) Sheng, X.; Himo, F. The Quantum Chemical Cluster Approach in Biocatalysis. *Acc. Chem. Res.* **2023**, acs.accounts.2c00795.
(50) The PyMOL Molecular Graphics System.
(51) Summers, T. J.; Daniel, B. P.; Cheng, Q.; DeYonker, N. J. Quantifying Inter-Residue Contacts through Interaction Energies. *J. Chem. Inf. Model.* **2019**, *59* (12), 5034–5044.
(52) Vennelakanti, V.; Nazemi, A.; Mehmood, R.; Steeves, A. H.; Kulik, H. J. Harder, Better, Faster, Stronger: Large-Scale QM and QM/MM for Predictive Modeling in Enzymes and Proteins. *Curr. Opin. Struct. Biol.* **2022**, *72*, 9–17.
(53) Sumner, S.; Söderhjelm, P.; Ryde, U. Effect of Geometry Optimizations on QM-Cluster and QM/MM Studies of Reaction Energies in Proteins. *J. Chem. Theory Comput.* **2013**, *9* (9), 4205–4214.
(54) Liao, R.-Z.; Thiel, W. Convergence in the QM-Only and QM/MM Modeling of Enzymatic Reactions: A Case Study for Acetylene Hydratase. *J. Comput. Chem.* **2013**, 2389–2397.
(55) Jindal, G.; Warshel, A. Exploring the Dependence of QM/MM Calculations of Enzyme Catalysis on the Size of the QM Region. *J. Phys. Chem. B* **2016**, *120* (37), 9913–9921.
(56) Kulik, H. J.; Zhang, J.; Klinman, J. P.; Martínez, T. J. How Large Should the QM Region Be in QM/MM Calculations? The Case of Catechol *O* -Methyltransferase. *J. Phys. Chem. B* **2016**, *120* (44), 11381–11394.
(57) Masson, P.; Bec, N.; Froment, M.-T.; Nachon, F.; Balny, C.; Lockridge, O.; Schopfer, L. M. Rate-Determining Step of Butyrylcholinesterase-Catalyzed Hydrolysis of Benzoylcholine and Benzoylthiocholine. Volumetric Study of Wild-Type and D70G Mutant Behaviour. *Eur. J. Biochem.* **2004**, *271* (10), 1980–1990.

(58) Lisi, G. P.; Currier, A. A.; Loria, J. P. Glutamine Hydrolysis by Imidazole Glycerol Phosphate Synthase Displays Temperature Dependent Allosteric Activation. *Front. Mol. Biosci.* **2018**, *5*, 4.
(59) Glendening, E. D.; Landis, C. R.; Weinhold, F. *NBO 7.0*: New Vistas in Localized and Delocalized Chemical Bonding Theory. *J. Comput. Chem.* **2019**, jcc.25873.
(60) Tantillo, D. J.; Jiangang, C.; Houk, K. N. Theozymes and Compuzymes: Theoretical Models for Biological Catalysis. *Curr. Opin. Chem. Biol.* **1998**, *2* (6), 743–750.
(61) Windsor, I. W.; Gold, B.; Raines, R. T. An $n \rightarrow \pi^*$ Interaction in the Bound Substrate of Aspartic Proteases Replicates the Oxyanion Hole. *ACS Catal.* **2019**, *9* (2), 1464–1471.
(62) Thoden, J. B.; Huang, X.; Raushel, F. M.; Holden, H. M. The Small Subunit of Carbamoyl Phosphate Synthetase: Snapshots along the Reaction Pathway. *Biochemistry* **1999**, *38* (49), 16158–16166.
(63) last, first. Gaussian 16 {R}evision {C}.01, 2019.
(64) Chai, J.-D.; Head-Gordon, M. Long-Range Corrected Hybrid Density Functionals with Damped Atom–Atom Dispersion Corrections. *Phys. Chem. Chem. Phys.* **2008**, *10* (44), 6615.
(65) Hehre, W. J.; Ditchfield, R.; Pople, J. A. Self—Consistent Molecular Orbital Methods. XII. Further Extensions of Gaussian—Type Basis Sets for Use in Molecular Orbital Studies of Organic Molecules. *J. Chem. Phys.* **1972**, *56* (5), 2257–2261.
(66) Hariharan, P. C.; Pople, J. A. The Influence of Polarization Functions on Molecular Orbital Hydrogenation Energies. *Theor. Chim. Acta* **1973**, *28* (3), 213–222.
(67) Becke, A. D. Density-functional Thermochemistry. III. The Role of Exact Exchange. *J. Chem. Phys.* **1993**, *98* (7), 5648–5652.
(68) Lee, C.; Yang, W.; Parr, R. G. Development of the Colle-Salvetti Correlation-Energy Formula into a Functional of the Electron Density. *Phys. Rev. B* **1988**, *37* (2), 785–789.
(69) Grimme, S.; Antony, J.; Ehrlich, S.; Krieg, H. A Consistent and Accurate *Ab Initio* Parametrization of Density Functional Dispersion Correction (DFT-D) for the 94 Elements H-Pu. *J. Chem. Phys.* **2010**, *132* (15), 154104.
(70) Grimme, S.; Ehrlich, S.; Goerigk, L. Effect of the Damping Function in Dispersion Corrected Density Functional Theory. *J. Comput. Chem.* **2011**, *32* (7), 1456–1465.
(71) Luque, F. J.; López, J. M.; Orozco, M. Perspective on "Electrostatic Interactions of a Solute with a Continuum. A Direct Utilization of Ab Initio Molecular Potentials for the Prevision of Solvent Effects." *Theor. Chem. Acc. Theory Comput. Model. Theor. Chim. Acta* **2000**, *103* (3–4), 343–345.
(72) Cossi, M.; Barone, V.; Cammi, R.; Tomasi, J. Ab Initio Study of Solvated Molecules: A New Implementation of the Polarizable Continuum Model. *Chem. Phys. Lett.* **1996**, *255* (4–6), 327–335.
(73) Himo, F. Recent Trends in Quantum Chemical Modeling of Enzymatic Reactions. *J. Am. Chem. Soc.* **2017**, *139* (20), 6780–6786.
(74) Blomberg, M. R. A. How Quantum Chemistry Can Solve Fundamental Problems in Bioenergetics. *Int. J. Quantum Chem.* **2015**, *115* (18), 1197–1201.
(75) Luchini, G.; Alegre-Requena, J. V.; Funes-Ardoiz, I.; Paton, R. S. GoodVibes: Automated Thermochemistry for Heterogeneous Computational Chemistry Data. *F1000Research* **2020**, *9*, 291.
(76) Kozuch, S.; Shaik, S. How to Conceptualize Catalytic Cycles? The Energetic Span Model. *Acc. Chem. Res.* **2011**, *44* (2), 101–110.
(77) Horn, P. R.; Mao, Y.; Head-Gordon, M. Probing Non-Covalent Interactions with a Second Generation Energy Decomposition Analysis Using Absolutely Localized Molecular Orbitals. *Phys. Chem. Chem. Phys.* **2016**, *18* (33), 23067–23079.
(78) Epifanovsky, E.; Gilbert, A. T. B.; Feng, X. Software for the Frontiers of Quantum Chemistry: An Overview of Developments in the Q-Chem 5 Package. *J. Chem.* **2021**.